



Physikalisch-Technische Bundesanstalt
National Metrology Institute

The following article is hosted by PTB;

DOI: 10.7795/810.20240617 It is provided for personal use only.

Physically Based Rendering Method to Derive Realistic Simulation of Chromatic Confocal Measurements

Dan Linnert, Manuel Stavridis, Ulrich Neuschaefer-Rube, Rainer Tutsch

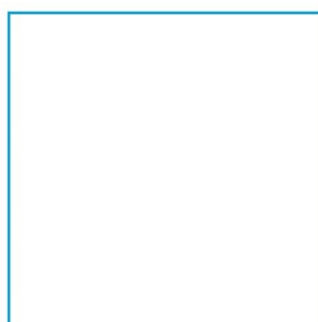
The paper is also available on the SPIE digital library: Dan Linnert, Manuel Stavridis, Ulrich Neuschaefer-Rube, Rainer Tutsch "Physically Based Rendering Method to Derive Realistic Simulation of Chromatic Confocal Measurements", Proc. SPIE 12619, Modeling Aspects in Optical Metrology IX, 126190Q (10 August 2023); <https://doi.org/10.1117/12.2673432>

COPYRIGHT 2023 Society of Photo-Optical Instrumentation Engineers (SPIE). One print or electronic copy may be made for personal use only. Systematic reproduction and distribution, duplication of any material in this paper for a fee or for commercial purposes, or modification of the content of the paper are prohibited.

Acknowledgement: The 20IND07 TracOptic project has received funding from the EMPIR programme co-financed by the Participating States and from the European Union's Horizon 2020 research and innovation programme.

Available at:

<https://doi.org/10.7795/810.20240617>



Physically Based Rendering Method to Derive Realistic Simulation of Chromatic Confocal Measurements

Dan Linnert^a, Manuel Stavridis^b, Ulrich Neuschaefer-Rube^a, Rainer Tutsch^c

^aPhysikalisch-Technische Bundesanstalt (PTB), Bundesallee 100, Braunschweig, Germany

^bPhysikalisch-Technische Bundesanstalt (PTB), Abbestraße 2-12 10587 Berlin, Germany

^cInstitut für Produktionsmesstechnik, TU Braunschweig, Schleinitzstr. 20, Braunschweig, Germany

ABSTRACT

One important cause for limited traceability in optical metrology is the presence of systematic measurement errors caused by the interaction of the sensor and the measured object. These effects are complex and influenced by many factors, hence, they may differ significantly even among similar measurement systems. This also implies, that it is usually necessary to model the whole measurement chain including the relevant characteristics of the measured surface.

We are currently developing a model of a chromatic confocal point sensor dedicated to simulate object-dependent systematic measurement errors and estimating task-specific measurement uncertainties. The simulations already cover all relevant fundamental aspects of the system, some important details are currently being developed. We recently introduced realistic reflection characteristics based on methods originating in physically based rendering. We show how to phenomenologically describe the light-object-interaction using bidirectional reflectance distribution functions and how the principle of Monte Carlo Ray Tracing can be adopted for this use case.

We can already show the general influence of surface curvature and slope and can qualitatively predict systematic effects. However, simulations using the current model still show clear deviations from measurement results. While some effects are caused by non-ideal characteristics of the real system, others are likely caused by the approximations within our model. Therefore, further investigations and model developments are pursued.

Keywords: optical metrology, modeling, ray tracing, BRDF, chromatic confocal, systematic errors, traceability

1. INTRODUCTION

Motivation

There is a growing need for fast and non-contact measurement techniques to improve efficiency and accuracy in industrial manufacturing processes and quality control as well as other applications in other fields, such as medicine and biology. One cluster of methods that meets these requirements is optical coordinate metrology. This encompasses a wide field of realisations of different measurement principles, that enable highly accurate determination of geometric features and surface properties of an object without the need for physical contact.

However, optical coordinate metrology measurements exhibit significant systematic measurement errors, depending on the measurement constellation [1]–[3]. These errors can occur due to various interacting factors, such as the general measurement principle, its specific realisation, specific settings of the instrument, the characteristics of the surface under test (SUT), and environmental influences. Systematic deviations are therefore highly individual and can vary greatly from case to case.

If significant errors are not corrected or at least considered in the measurement uncertainty analysis, traceability of the measurement cannot be achieved. This leads to problems in quality assurance and manufacturing capability and can lead to an overall loss of confidence in the measurement results.

To address this problem, intensive research is being conducted in many places to develop models for such measurement processes [4], [5]. Modeling plays a crucial role in correcting the systematic errors and improving the measurement uncertainty. In this paper, we specifically consider the modeling of a chromatic confocal distance sensor. The presented model is based on ray tracing and uses methods adapted from physically based rendering to predict systematic errors.

Chromatic Confocal Measurement Principle

Before addressing the instrument model, the real instrument and its measuring principle will be explained. The instrument consists of a controller and a sensor head connected via a common graded index multimode fibre. White light is provided by a halogen lamp and guided to the sensor head, which consists of a system of lenses. The light emitted at the exit facet of the optical fibre is focused onto the SUT located within the measuring range. However, as the optical system comes with a deliberate strong chromatic aberration, only a small spectral bandwidth will be in focus. The light is scattered at the surface and the intensity distribution is imaged onto the plane of the same fibre interface from which the light originated. As the fibre end facet now acts as a filtering pinhole, spectral components that are out of focus are effectively blocked, as most of the light is outside the fibre aperture. The received light is analysed with a spectrometer which is connected to the optical fibre via a fibre coupler. Its signal exhibits a defined confocal peak. The location of this peak within the spectrum is determined using a dedicated algorithm, e.g., based on its centre of gravity. By calibration of the sensor, a response curve is established, enabling the conversion between focal wavelength and the distance between the sensor head and the SUT.

This type of sensor is suitable for various applications. This specific way of realizing a chromatic confocal instrument, has the advantage of having a passive sensor head, i.e., sources of thermal energy are physically separated. In our case, it is mounted on a coordinate measuring machine with three translatory axes. This allows a flexible usage, and the combined system enables measurements of 3D coordinates. Table 1 provides some specifications that shall help to assess the instrument's capabilities and therefore our achieved results, too.

Table 1. Sensor specifications

Sensor Specifications	
Measuring range	300 μm
Working distance	4.5 mm
Axial resolution	10 nm
Spot diameter	5 μm
Numerical aperture	0.50
Fiber core diameter	50 μm

2. METHODOLOGY

Ray tracing in Rendering

In Ray tracing the behaviour of light is simulated by following the path of individual rays of light as they interact with objects in a scene. It should be noted, however, that while ray tracing is based on the principles of geometrical optics, it does not consider the wave-optical or quantum mechanical properties of light. Instead, light is assumed to propagate in straight lines and the wavelike nature of light can be neglected for the purposes of the representation. This approach allows for realistic simulations of light and shadow in many virtual environments but has its limitations when it comes to accurately representing certain optical phenomena such as diffraction or interference effects.

Ray tracing is a common tool used in computer graphics for rendering of 3D scenes. Hence, a lot of ray tracing algorithms have been developed by that community. The application of ray tracing in computer graphics began in the 1970s [6] and was further developed in the following decades.

The rendering equation (1) [7] forms the mathematical basis of such ray tracing methods. It describes the relationship between the incident light, the reflections, and the emitted radiance L_e of a surface point. Latter is zero for all objects not emitting light by themselves. Dropping the emittance term leaves us with what is usually called the reflection equation. The equation further considers the incident radiance L_i from direction ω_i at a surface location \mathbf{x} with a local surface normal \mathbf{n} to calculate the outgoing radiance L_o . The material properties of the surface are represented by a bidirectional reflectance distribution function (BRDF) f_r , phenomenologically describing how much light (radiance) is reflected into a single direction considering incoming light (irradiance) from a given direction. All mentioned terms might depend on the wavelength of light λ . As the incoming rays have different directions of incidence, each one must be weighted with the

cosine of its incidence angle, which is calculated by the dot product of the direction vector and the surface normal. The integral in the rendering equation states, that all incidence directions across the hemisphere Ω must be considered.

$$L_o(\mathbf{x}, \omega_o, \lambda) = L_e(\mathbf{x}, \omega_o, \lambda) + \int_{\Omega} f_r(\mathbf{x}, \omega_i, \omega_o, \lambda) * L_i(\mathbf{x}, \omega_i, \lambda) * (\omega_i \cdot \mathbf{n}) d\omega_i \quad (1)$$

Different ray-tracing methods can usually be described as approaches to solve this integral. This is often done using a Monte Carlo approach, i.e., methods that are based on evaluations of the function at multiple randomly chosen supporting points. In the application for ray tracing this means computing many rays in different, random direction across the hemisphere evaluating the rendering equation for each ray. This technique is nowadays almost always used with importance sampling [8], ensuring that more rays are computed along more significant directions to increase the algorithm's efficiency.

A significant milestone was the introduction of what is known as Physically Based Rendering (PBR) in the 1980s [6], which introduced concepts of Helmholtz reciprocity and energy conservation. Helmholtz reciprocity states that the propagation directions can be inverted without changing the outcome of any calculations. In other words, the reflected or transmitted radiant flux is independent of whether the light travels from the source to the surface or from the surface to the source. In fact, in rendering rays are often traced in the opposite direction of light propagation or in a combination like bi-directional path tracing [9]. Energy conservation states that the total energy of incident light striking a surface is conserved. This means that the sum of reflected, absorbed, and transmitted light rays cannot exceed the energy of the incident ray. These principles form the basis for the accurate calculation of reflections – using physically based BRDF models – and transmissions in PBR.

Reflection model

In the first version of our model, only ideal specular and ideal diffuse (Lambertian) reflection had been implemented. Originally it was planned to implement a data driven reflection model [10] to simulate measurements at material standard specifically designed and characterised for this application. Due to delays realising this standard, we cannot present it here and have instead decided to continue by integrating a physically based BRDF model, so that we can simulate more realistic scattering characteristics.

The BRDF we are using is based on the Cook-Torrance model (2) [11] which is used in rendering to approximate scattering from rough surfaces. It assumes that the surface consists of microfacets with specular reflection characteristic, which makes it especially suitable to model metallic surfaces, though it should be noted that wavelength dependencies have not yet been implemented.

$$f_{r,cook-torrance}(\omega_i, \omega_o) = \frac{F * D * G}{4 * \cos \theta_i * \sin \theta_o} \quad (2)$$

The model is comprised of four different factors. The whole denominator is a normalisation factor which ensures energy conservation. The Fresnel term (3) determines how much light is reflected based on the Schlick approximation [12] and the materials refraction index n_r . This approximation would be abandoned once we decide to introduce wavelength dependency. The normal distribution function D – not to be mistaken with a normal distribution – statistically describes the orientation of the microfacets. We implemented the GG-X distribution (4) [13], [14], which is adjusted using the parameter α which is the square root of twice the RMS of the microfacets' slopes. θ_h meanwhile is the angle between the surface normal and the half-vector between incident and outgoing direction (cf. figure 1). In a microfacet BRDF model it further corresponds to the normal of a microfacet. The half-vector is also commonly used for isotropic BRDFs as it lowers its dimension by one and effectively reduces the computational effort and the size of BRDF measurement data [15]. The last term G handles masking and shadowing, considering that on a rough surface light might not reach parts of the surface due to self-shading and reflected light might not propagate to the outgoing direction also due to being blocked by another facet. We implemented the height-correlated Smith function G (5) [16], which combines the functions for masking and shadowing (6-7). They are calculated based on the roughness parameter a (8), which could be interpreted as an effective roughness based on the viewing or illumination angle and the surface roughness α .

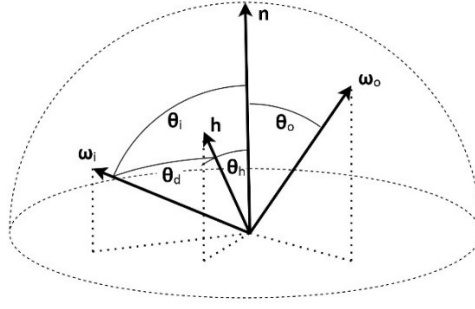


Figure 1. Spherical coordinate system following [15].

$$F = F_0 + (1 - F_0) * (1 - \cos \theta_i)^5 \text{ with } F_0 = \left(\frac{n_r - 1}{n_r + 1} \right)^2 \quad (3)$$

$$D = D_{GGX} = \frac{\alpha^2}{\pi((\alpha^2 - 1) \cos^2 \theta_h + 1)^2} \quad (4)$$

$$G = \frac{1}{1 + G_{1,i} + G_{1,o}} \quad (5)$$

$$G_{1,j} = \frac{1}{1 + \lambda_{GGX}(a_j)} \text{ with } j = i, o \quad (6)$$

$$\lambda_{GGX}(a_j) = \frac{-1 + \sqrt{1 + \frac{1}{a_j^2}}}{2} \quad (7)$$

$$a_j = \frac{\cos \theta_j}{\alpha \sqrt{1 - \cos^2 \theta_j}} \quad (8)$$

This microfacet model can be combined with a diffuse model, e.g., Lambertian reflection. Anyhow, in all simulations shown here we assumed that all light is being reflected following the Cook-Torrance model and is not scattered diffusely. Further, we used a refraction index of 2.8 for all simulations. This number does not represent a specific material but was chosen to represent a not-specified metallic material. Figure 2 shows two examples that illustrate the reflection lobe, that is described by such type of BRDF.

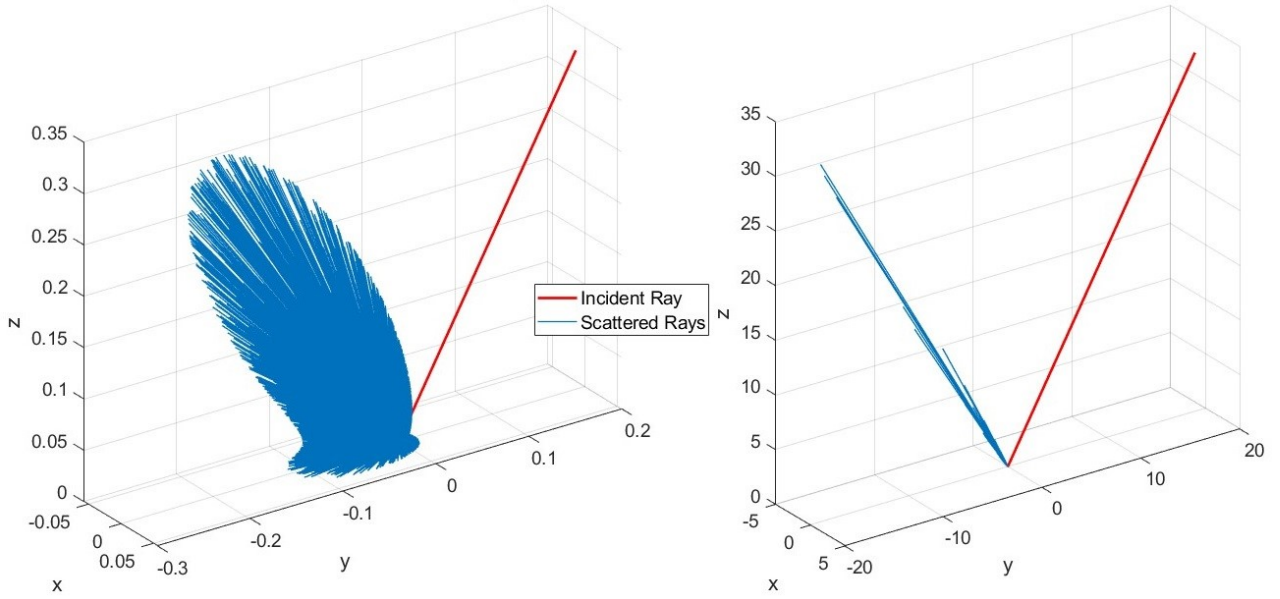


Figure 2. Visualization of the implemented Cook-Torrance BRDF model across the whole hemisphere for an incident angle of 30° . Left: $\alpha = 0.25$ which corresponds to a RMS of the microfacets' slopes of approximately 1.8° . Right: $\alpha = 0.025$ which corresponds to a RMS of the microfacets' slopes of approximately 0.018° . Note that the scaling is different for both depictions for better visibility of details.

Importance Sampling

Importance sampling means that we sample our function more often at more relevant locations. Applied for ray tracing this means that we should select our samples following a probability distribution function that matches the BRDF. To compensate for the biases introduced by this type of sampling, we need to weight these samples by the inverse of their probability. Hence, importance sampling can significantly improve the overall efficiency of our algorithm, but it can also lead to biased results, if not handled appropriately. Therefore, this section will briefly describe how our directions are sampled and how the corresponding weights are calculated.

The algorithm we use is based on the microfacet normal distribution D (4). As this term is dominant within the BRDF, especially for the directions we evaluate, it is considered a good choice. By applying the inversion method, equations can be derived to sample the microfacets' azimuth angles Φ (9) and their polar angles Θ (10) [14], where ζ_i represents a random number between zero and one, uniformly sampled.

$$\Phi = 2\pi\zeta_\phi \quad (9)$$

$$\Theta = \cos \sqrt{\frac{1 - \zeta_\theta}{\zeta_\theta(\alpha^2 - 1) + 1}} \quad (10)$$

Our algorithm further features the possibility to filter by outgoing direction, to dismiss rays that miss the sensor aperture after being reflected at a microfacet. This is done by drawing samples until we either end up with a specified number of accepted rays or stop after certain number of total drawn samples. As this can also be described as applying a second probability distribution that is equal within our acceptance cone and zero everywhere else, this can be called multiple importance sampling [17].

If we scale D by dividing by $4 \cdot \cos(\theta_d)$, its reciprocal can be used as weight [6]. However, if the algorithm described in the previous paragraph is used, scaling of weights is required. For each intersection point we are dividing each weight by the sum of all weights we have drawn – accepted or dismissed – which is also known as balance heuristics [6]. Figure 3

visualizes how the rays are sampled for one single incoming ray. In the bottom left plot, we can see the effect of filtering, which dismisses rays outside a circular aperture. We expect that in this case almost all rays will reach the sensor's fibre plane. In the upper case we would expect that more than half of the rays will be blocked by an aperture.

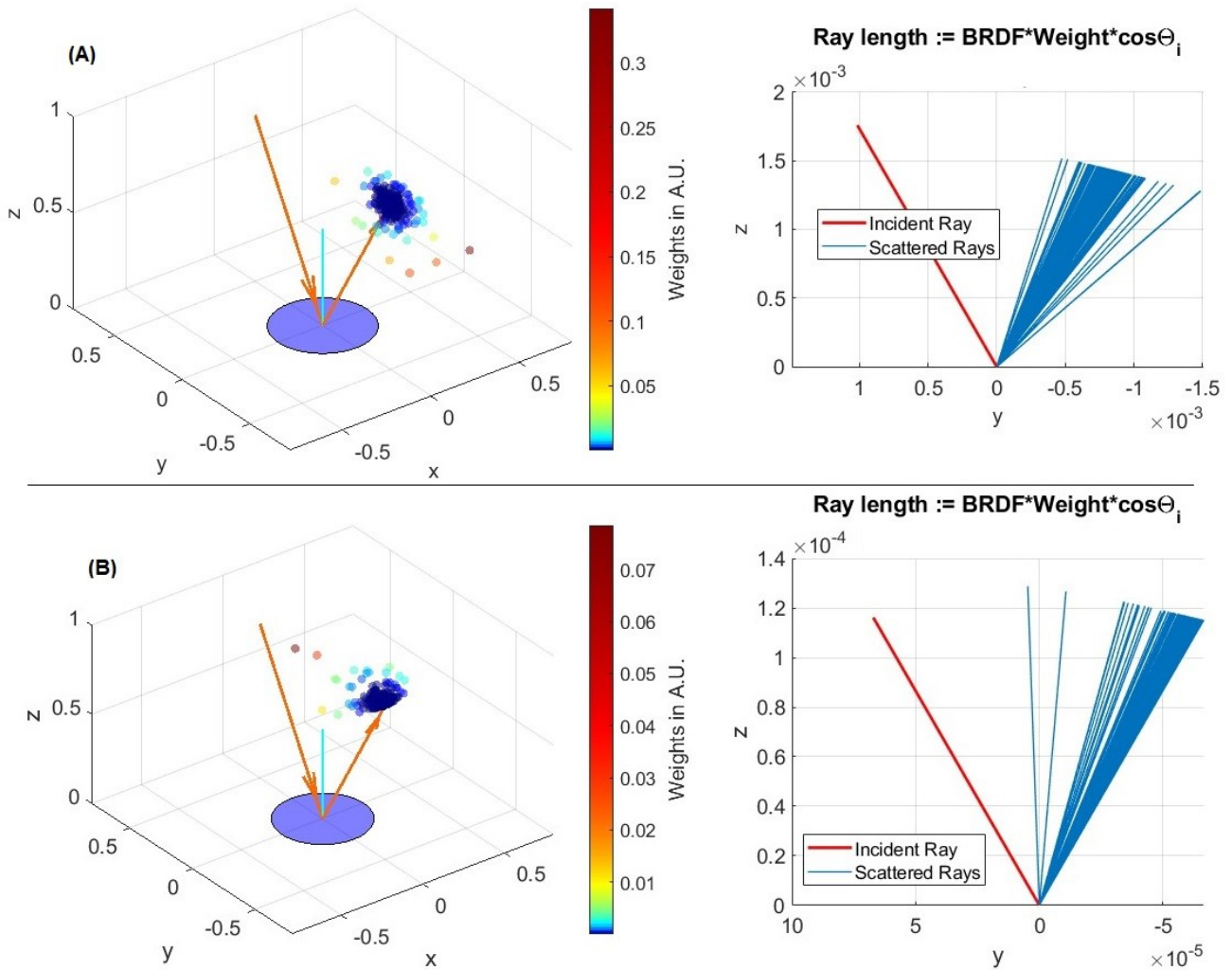


Figure 3. Visualization of the implemented importance (A) and multiple importance (B) sampling at a single intersection point and an incident angle of 30° . 256 random rays were drawn using the described algorithm. The roughness term α was set to 0.02, which models a relatively smooth surface with a distinct specular reflex. The left plots show the incoming and specular direction as orange arrows, the SUT as a disc including its normal as a cyan line. The dots represent the sampled directions. The right plots essentially show the radiance associated with each ray represented by its length. Note that the colorbars and the right plots are scaled differently for better visibility of details.

3. APPLYING RAY TRACING TO SIMULATE CHROMATIC CONFOCAL MEASUREMENTS

While ray tracing and optical simulations in general have been used in the context of optical metrology and chromatic confocal microscopy for some time, e.g., to design or improve optical systems or as part of the measurement evaluation, the issue of significant workpiece-dependent measurement errors has not been solved to a satisfactory level. To better understand such effects, preferably correct them and identify ways to incorporate them in uncertainty evaluations, we are setting up a model of a chromatic confocal distance sensor. While we have plans to combine our model with a wave optical

scattering model – provided by our research partners – to achieve a hybrid model similar to [18], this article will focus on our current work which stays within the bounds of geometrical optics and PBR.

To avoid having to start from scratch, we are using a code library for MATLAB® called SimOptDevice [19]. It provides a variety of classes and algorithms to model and simulate optical experiments. As it is developed at PTB, we have full access to all implementations granting us full flexibility. As it is and has been used in several different projects across our institute, the core algorithms are well tested and therefore provide a solid basis for our implementation.

Although other approaches are still in consideration for future developments, we are exclusively tracing the rays following the propagation direction of light. More precisely, we start the simulation at the fibre interface and not at the light source itself. While in classical confocal microscopy models the illumination may often be assumed to be coming from an ideal point source, this is an oversimplification in this case, as the chromatic confocal instruments have a larger pinhole diameter. Hence, we are currently casting random rays starting at random positions and aiming at random directions. While the starting points are limited to a circular plane representing the fibre exit facet, the starting directions are limited by the approximate image side numerical aperture of the lens system as it is significantly smaller than the numerical aperture of the optical fibre. Both aspects are sampled following uniform distribution, however, each ray is associated with an intensity value, which may be varied based on location and direction to match a more realistic overall radiance distribution as they are, for example, described in [20], [21].

To simulate the light propagation through the optic, the casted rays are traced following the Fresnel equations. As this is handled by algorithms implemented in SimOptDevice we primarily want to refer to [19] for further information. What has been added as part of this modeling project is chromatic dispersion. To describe the wavelength dependency of the refractive indices of the lens materials, we use the Sellmeier equation (11) for most lenses, which is parameterized by data sheet entries provided by the corresponding glass manufacturers. As the so-called absorption resonance wavelengths equal to $\sqrt{C_i}$ are all clearly outside our applied wavelength range, this model provides a good basis for this simulation. For the lens with high chromatic aberration a 6-term SCHOTT® model (12) is used instead.

$$n^2(\lambda) = 1 + \sum_{i=1}^3 \frac{B_i \lambda^2}{\lambda^2 - C_i} \quad (11)$$

$$n^2(\lambda) = A_0 + A_1 \lambda^2 + \sum_{i=1}^4 \frac{A_{i+1}}{\lambda^{2i}} \quad (12)$$

Applying these models, we sequentially trace ray bundles associated with different wavelengths through our optical system. The selection of wavelengths is usually done automatically based on the pre-set distance of the sensor relative to the SUT model and the response curve of our model. Also, the used sampling wavelengths, correspond with the sampling points of the integrated spectrometer.

Having calculated intersection points and illumination directions at the SUT for all relevant wavelengths, we currently deal with each point separately. Casting many reflection rays for every single incoming ray, applying the BRDF to determine each ray's radiance typically takes about 10 % of the processing time. When simulating at high slopes that cause many specular reflection directions missing the system aperture by a high margin, the computational effort can increase significantly as many samples will be discarded. Additionally, tracing the huge number of scattered rays back to the fibre interface is usually even more expensive. Therefore, this aspect could be subject to change soon.

Anyhow, as stated, we currently apply the same algorithm to each intersection point. A certain number of rays inside the systems aperture is computed for each intersection – this is done by importance sampling as described. We trace those rays back to the fibre interface and evaluate which rays are within the aperture and therefore contribute to the spectrometer signal. Then we apply the BRDF to find each ray's intensity. By tracking many rays to simulate the illumination of the SUT, we approximate the integral of the reflectance equation for the entire measurement spot. Casting multiple scattering rays across the aperture, which corresponds to a solid angle Ψ , can be mathematically described (13) by adjusting the rendering equation (1). As we do this at many intersection points, we basically use a Monte Carlo approach to integrate over the solid angle in front of detection pinhole as well as over the pinhole area to determine the incident light intensity.

$$L_o(\mathbf{x}, \Psi \subseteq \Omega, \lambda) = \int_{\Psi \subseteq \Omega} f_r(\omega_i, \omega_o) * L_i(\mathbf{x}, \omega_i, \lambda) * (\omega_i \cdot \mathbf{n}) d\omega_o \quad (13)$$

The behaviour of the spectrometer itself is currently not simulated, so we analyse the signal we just obtained. We have detailed information about the optics, but besides the applied response curve we have no inside knowledge about the algorithms applied, nor did we have the possibility to analyse the simulated signal using the evaluation on the controller itself. As for all results shown here, we have used a basic centre of gravity algorithm – applied to all sampling points with an intensity of at least 50 % of the maximum intensity – to determine the focal wavelength. To translate this into an actual distance, we apply a reference curve that was obtained by simulating the calibration procedure using our model, so that it is consistent within itself.

4. EARLY SIMULATION RESULTS

In this section, we aim to evaluate the performance of our ray tracing model by comparing simulated and measured data. We focus on sphere measurements as their geometry exhibits a continuous spectrum of slope angles, which significantly impacts our simulation results, as previously demonstrated [22]. For the cases presented below, we expect that the reflection characteristics will play a crucial role in determining the outcomes. Until recently, our simulations could not accurately capture these reflection behaviors. Meanwhile, with the newly implemented techniques described in the preceding chapters, we can now simulate more realistic reflection behavior. However, we do not anticipate the surface curvature – all spheres have a nominal radius of 10 mm – to have a noticeable impact on these measurements and simulations.

Figure 4 displays plots of radial residuals obtained from least-square circle fits to both simulation and measurement data collected during a scan across the sphere pole. Although we performed simulations with different settings, the results presented here represent the overall behavior well. It is evident that both simulation and measurement exhibit a distinct dip in residuals at a surface slope of approximately 20°. This behavior seems to be a characteristic of our system design, effectively captured by our model. However, there are noticeable differences, such as the dip observed at around 5 to 10° in the simulation. Additionally, the measurements exhibit higher residuals, which are likely attributed to non-idealities in the real system introducing additional systematic errors. Finally, we cannot determine whether the residuals of the simulation flatten out beyond 30° or not. We refrained from simulating at higher slopes due to increased noise and highly fluctuating intensity values above 20°. Moreover, simulating points at higher slopes requires a significant amount of time due to our sampling strategy. Noise is currently a general issue, as indicated by occasional outliers in the spectrometer signal intensities even at lower slopes. Our current approach of evaluating the center-of-gravity does not handle these outliers well.

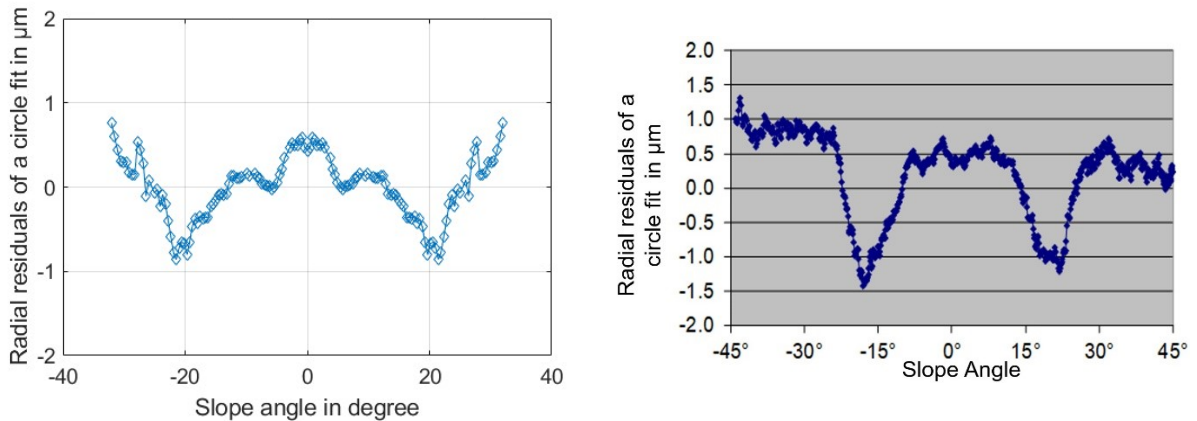


Figure 4. Left: Simulation results using an ideal sensor model to measure a surface with moderate roughness ($\alpha = 0.02$). Only the measurement of the left half was simulated, the points are mirrored at the pole, outliers have been removed and the residuals have been smoothed using a moving mean filter of size three. 100k rays were traced to the SUT, where 128 scattered rays were created per incoming ray. Right: Real measurement of a shiny metal sphere with moderate roughness.

The measurement result shown in Figure 4 right was obtained from previous measurements, and since then, we have replaced the sensor head. Although both systems share the same nominal design, we recently made an interesting discovery with our current system: it exhibits noticeable asymmetrical residuals when measuring spheres. However, it is important to note that the overall systematic effect is significantly smaller when measuring the same sphere (Figure 5, left) which was the original reason to change it. Nevertheless, the asymmetry remains visible and occurs similarly when measuring spheres with more specular surface characteristics (Figure 5, right). We suspect that a non-ideal lens adjustment is the primary cause of this asymmetry. While we expect the effect to be a combination of different error sources, we believe that the adjustment of the lens closest to the SUT has a particular strong influence.

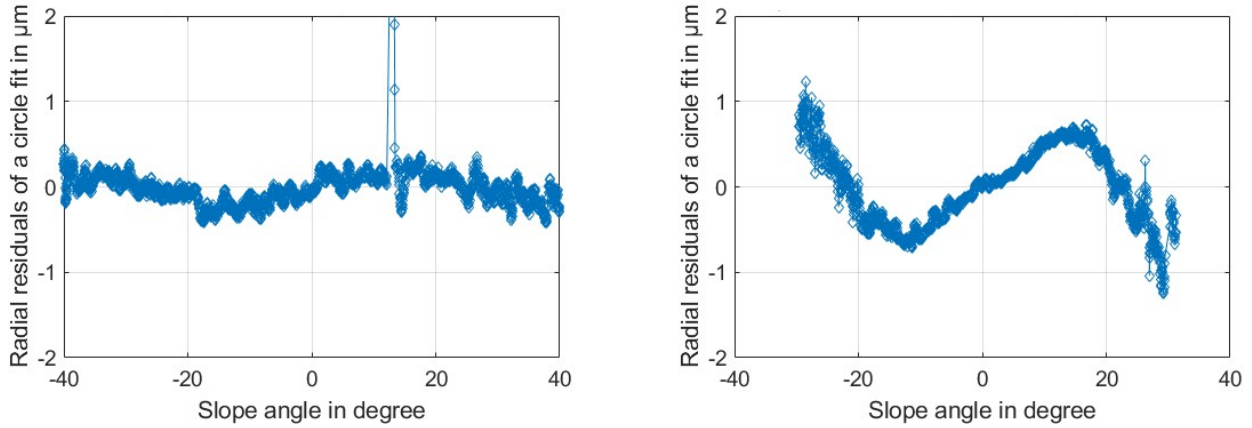


Figure 5. Radial residuals of sphere measurements across a sphere pole. Left: Measurement of a rough metal sphere with shiny reflexion characteristic. The outliers seen at about 15° seem to be caused by a particle on the surface. Right: Measurement of a smooth metal sphere with specular reflexion characteristic.

To explore this further, we conducted simulations of a specular sphere with a misaligned lens, as depicted in Figure 6. By simulating ideal specular reflection, we can compare these results with the right plot of Figure 5. In the simulations, we observed that the residuals are more rounded off or less distinct, and overall, they are smaller compared to the measurements. However, it is important to note that we cannot currently provide specific details about actual misalignments or other factors that might contribute significantly to the observed effect in the measurements. Nonetheless, our overall conclusion is positive: we have successfully replicated the effect using our sensor model by introducing a lateral offset to the last lens.

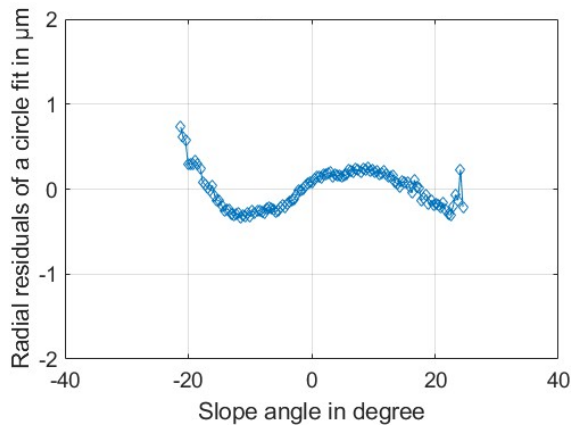


Figure 6. Radial residuals of a sphere measurement simulation. The lens closest to the SUT was moved off the original optical axis by 150 μm in x-direction. The surface was modelled to be specular.

5. CONCLUSIONS

We successfully implemented a ray tracing model to accurately simulate point measurements using a chromatic confocal distance sensor. By incorporating the Cook-Torrance BRDF model and the GG-X microfacet distribution, we effectively introduced more realistic scattering characteristics compared to ideal specular and diffuse reflection. Our adjusted importance sampling strategy enabled us to simulate the measurement process and predict major object dependent effects. This demonstrates the potential of our model to provide valuable insights into real-world scenarios. While our simulations currently exhibit significant noise and outliers, resulting in deviations from expected outcomes, we recognize the need for further algorithm development. Future enhancements, such as incorporating diffraction into our model, will also address these limitations. Additionally, we observed variations in behavior among real sensors of the same type, some of which are strongly asymmetric. We were already able to simulate such an effect by introducing a lens misalignment to the sensor model. We will further incorporate additional sensor characteristics, enabling our model to accurately represent such real-world variations. Moving forward, we plan to conduct comprehensive comparisons between simulations and measurements on a signal basis. This will allow us to evaluate the performance of our model and further refine our understanding of the underlying factors. Furthermore, it will help us to adjust the evaluation to better match the actual evaluation performed on the instrument controller.

ACKNOWLEDGEMENT

The 20IND07 TracOptic project has received funding from the EMPIR programme co-financed by the Participating States and from the European Union's Horizon 2020 research and innovation programme.

REFERENCES

- [1] H. Noura, N. El-Hayek, X. Yuan, and N. Anwer, 'Characterization of the main error sources of chromatic confocal probes for dimensional measurement', *Meas. Sci. Technol.*, vol. 25, no. 4, p. 044011, Apr. 2014, doi: 10.1088/0957-0233/25/4/044011.
- [2] M. Rahlves, B. Roth, and E. Reithmeier, 'Systematic errors on curved microstructures caused by aberrations in confocal surface metrology', *Opt. Express, OE*, vol. 23, no. 8, pp. 9640–9648, Apr. 2015, doi: 10.1364/OE.23.009640.
- [3] R. Su, Y. Wang, J. Coupland, and R. Leach, 'On tilt and curvature dependent errors and the calibration of coherence scanning interferometry', *Opt. Express*, vol. 25, no. 4, p. 3297, Feb. 2017, doi: 10.1364/OE.25.003297.
- [4] P.-E. Hansen and L. Siaudinyte, 'A virtual microscope for simulation of Nanostructures', *EPJ Web Conf.*, vol. 266, p. 10004, 2022, doi: 10.1051/epjconf/202226610004.
- [5] P. de Groot, X. C. de Lega, R. Su, J. Coupland, and R. Leach, 'Fourier optics modelling of coherence scanning interferometers', in *Applied Optical Metrology IV*, SPIE, Aug. 2021, pp. 107–126. doi: 10.1117/12.2595668.
- [6] M. Pharr, W. Jakob, and G. Humphreys, *Physically Based Rendering: From Theory to Implementation*, 3rd ed. Cambridge, MA: Morgan Kaufmann, 2016.
- [7] J. T. Kajiya, 'The Rendering Equation', *SIGGRAPH '86: Proceedings of the 13th annual conference on Computer graphics and interactive techniques*, vol. 20, no. 4, pp. 143–150, 1986, doi: 10.1145/15922.15902.
- [8] R. L. Cook, T. Porter, and L. Carpenter, 'Distributed ray tracing', *SIGGRAPH '84: Proceedings of the 11th annual conference on Computer graphics and interactive techniques*, vol. 18, no. 3, pp. 137–145, 1984.
- [9] E. Veach, 'Robust Monte Carlo Methods for Light Transport Simulation'. Stanford University, 1997.
- [10] W. Matusik, 'A data-driven reflectance model', Thesis, Massachusetts Institute of Technology, 2003. Available at: <https://dspace.mit.edu/handle/1721.1/87454>
- [11] R. L. Cook and K. E. Torrance, 'A Reflectance Model for Computer Graphics', *ACM Trans. Graph.*, vol. 1, no. 1, pp. 7–24, 1982, doi: 10.1145/357290.357293.
- [12] C. Schlick, 'An Inexpensive BRDF Model for Physically-based Rendering', *Computer Graphics Forum*, vol. 13, no. 3, pp. 233–246, 1994, doi: 10.1111/1467-8659.1330233.
- [13] T. S. Trowbridge and K. P. Reitz, 'Average irregularity representation of a rough surface for ray reflection', *J. Opt. Soc. Am., JOS A*, vol. 65, no. 5, pp. 531–536, 1975, doi: 10.1364/JOSA.65.000531.

- [14] B. Walter, S. R. Marschner, H. Li, and K. E. Torrance, 'Microfacet Models for Refraction through Rough Surfaces', *Proceedings of the 18th Eurographics conference on Rendering Techniques*, pp. 195–206, 2007.
- [15] S. M. Rusinkiewicz, 'A New Change of Variables for Efficient BRDF Representation', *Proceedings of the Eurographics Rendering Workshop*, pp. 11–23, 1998, doi: 10.1007/978-3-7091-6453-2_2.
- [16] S. Lagarde and C. de Rousiers, 'Moving Frostbite to Physically Based Rendering 3.0', 2014. Accessed: Jun. 02, 2023. [Online]. Available at: <https://seblagarde.wordpress.com/tag/physically-based-rendering/>
- [17] E. Veach and L. J. Guibas, 'Optimally combining sampling techniques for Monte Carlo rendering', in *Proceedings of the 22nd annual conference on Computer graphics and interactive techniques - SIGGRAPH '95*, Not Known: ACM Press, 1995, pp. 419–428. doi: 10.1145/218380.218498.
- [18] M. Hillenbrand, 'Confocal systems for spectral information coding', Thesis, TU Ilmenau, 2016. Available at: https://www.db-thueringen.de/servlets/MCRFileNodeServlet/dbt_derivate_00033167/ilm1-2016000026.pdf
- [19] R. Schachtschneider, M. Stavridis, I. Fortmeier, M. Schulz, and C. Elster, 'SimOptDevice: a library for virtual optical experiments', *J. Sens. Sens. Syst.*, vol. 8, no. 1, pp. 105–110, Feb. 2019, doi: 10.5194/jsss-8-105-2019.
- [20] A. Asadpour and H. Golnabi, 'Fiber Output Beam Shape Study Using Imaging Technique', *J. of Applied Sciences*, vol. 10, no. 4, pp. 312–318, Feb. 2010, doi: 10.3923/jas.2010.312.318.
- [21] K. Horiguchi, S. Kobayashi, and O. Sugihara, 'Calculation Model for Multimode Fiber Connection Using Measured Near- and Far-Field Patterns', *IEEE Photonics Technology Letters*, vol. 33, no. 6, pp. 285–288, Mar. 2021, doi: 10.1109/LPT.2021.3057129.
- [22] D. Linnert, U. Neuschaefer-Rube, and M. Stavridis, 'Development of a Chromatic Confocal Sensor Model Dedicated to Investigating Object-Dependent Effects', in *Proceedings of SMSI, Nürnberg*, May 2023, pp. 276–277. doi: 10.5162/SMSI2023/E7.3.